A&A 609, A49 (2018)
DOI: 10.1051/0004-6361/201731699

Astronomy & Astrophysics

Gas and galaxies in filaments between clusters of galaxies

The study of A399-A401

V. Bonjean[1,2], N. Aghanim[1], P. Salomé[2], M. Douspis[1], and A. Beelen[1]

[1] Institut d'Astrophysique Spatiale, CNRS (UMR 8617), Université Paris-Sud, Bâtiment 121, Orsay, France
e-mail: victor.bonjean@ias.u-psud.fr
[2] LERMA, Observatoire de Paris, PSL Research University, CNRS, Sorbonne Universités, UPMC Univ. Paris 06, 75014 Paris, France

Received 2 August 2017 / Accepted 23 October 2017

ABSTRACT

We have performed a multi-wavelength analysis of two galaxy cluster systems selected with the thermal Sunyaev-Zel'dovich (tSZ) effect and composed of cluster pairs and an inter-cluster filament. We have focused on one pair of particular interest: A399-A401 at redshift $z \sim 0.073$ seperated by 3 Mpc. We have also performed the first analysis of one lower-significance newly associated pair: A21-PSZ2 G114.09-34.34 at $z \sim 0.094$, separated by 4.2 Mpc. We have characterised the intra-cluster gas using the tSZ signal from *Planck* and, when possible, the galaxy optical and infrared (IR) properties based on two photometric redshift catalogues: 2MPZ and WISExSCOS. From the tSZ data, we measured the gas pressure in the clusters and in the inter-cluster filaments. In the case of A399-A401, the results are in perfect agreement with previous studies and, using the temperature measured from the X-rays, we further estimate the gas density in the filament and find $n_0 = (4.3 \pm 0.7) \times 10^{-4}$ cm^{-3}. The optical and IR colour–colour and colour–magnitude analyses of the galaxies selected in the cluster system, together with their star formation rate, show no segregation between galaxy populations, both in the clusters and in the filament of A399-A401. Galaxies are all passive, early type, and red and dead. The gas and galaxy properties of this system suggest that the whole system formed at the same time and corresponds to a pre-merger, with a cosmic filament gas heated by the collapse. For the other cluster system, the tSZ analysis was performed and the pressure in the clusters and in the inter-cluster filament was constrained. However, the limited or nonexistent optical and IR data prevent us from concluding on the presence of an actual cosmic filament or from proposing a scenario.

Key words. galaxies: clusters: individual: A399 – galaxies: clusters: individual: A401 – cosmology: observations – large-scale structure of Universe

1. Introduction

Cosmic structures are formed through accretion of matter, from the small-scale quantum fluctuations in the very early Universe to the tens of Mpc-scale filaments and super-clusters. This scenario was largely corroborated by cosmological numerical simulations such as Millenium (Springel et al. 2005), Horizon (Teyssier et al. 2009), or Illustris (Vogelsberger et al. 2014), reproducing the evolution of the 80% dark matter (DM) content of the universe. Observations from large surveys (e.g. SDSS, Tempel et al. 2014; GAMA, Alpaslan et al. 2014) allow us to probe the large-scale distribution of galaxies that amount to 4% of the universe in the form of cold baryons (cold gas and stars in galaxies). The warm-hot and hot gas represents the remaining 16% of matter. Both simulations and observation indicate that matter is distributed in the form of a cosmic web, an ensemble of interconnected filaments, sheets, and voids. The baryonic matter flows along the gravitational potential well of DM filaments into the connecting nodes of the cosmic web: the galaxy clusters, where the gas is virialised and heated up to high temperatures (of order 10^8 K).

As they are built up over time from mergers and interactions of smaller systems (e.g., Navarro et al. 1995; Springel et al. 2005), galaxy clusters are naturally connected to the cosmic web via the filaments. Strategies to probe the cosmic web are thus associated with our ability to probe filamentary structures between clusters or in their outskirts. This is in principle possible via observation of the galaxy distribution, the weak gravitational lensing, the X-ray emission from hot gas, and the thermal Sunyaev-Zel'dovich (tSZ) effect (Sunyaev & Zeldovich 1969), but the search for filaments linking the clusters to the cosmic web is hard. This subject has gained a lot of interest, and focuses mostly on two cases: filaments in the outskirts of individual clusters and inter-cluster filaments (or bridges) in pairs of clusters. Regarding the former case, Eckert et al. (2015) detected large-scale structures of several Mpc in the outskirts of the galaxy cluster Abell 2744 at redshift $z = 0.306$, combining observations of the X-ray emission, galaxy over-densities, and weak lensing. For the DAFT/FADA cluster sample (Guennou et al. 2010), Durret et al. (2016) searched for and found filaments in clusters' outskirts with two-dimensional (2D) galaxy densities obtained with CFHT and Subaru observations. Regarding cluster pairs, the inter-cluster filament or the bridge is expected to be denser with a hotter gas, and thus in principle easier to detect, in particular in the X-rays and tSZ effect (Dolag et al. 2006). Cluster pairs are thus good targets and have therefore been the subject of numerous studies. The photometric properties of the galaxies in the inter-cluster filament, their star-formation evolution, their weak lensing properties, and so on, were performed in many selected cluster (or group) pairs (e.g. Fadda et al. 2008; Gallazzi et al. 2009; Edwards et al. 2010; Zhang et al. 2013; Martínez et al. 2016; Epps & Hudson 2017). Galaxy clusters

may show substructures or evidence of dynamical effect: they merge, interact, and accrete smaller groups. The galaxy properties derived from optical and near-infrared data thus need to be combined, in a multi-wavelength analysis, with the study of cluster gas content. The gas properties of cluster pairs were therefore also investigated mostly using X-ray observations. This is the case of the particular pair Abell 399–Abell 401, thoroughly studied using data from ASCA, ROSAT, Suzaku and *XMM-Newton* (e.g. Karachentsev & Kopylov 1980; Ulmer & Cruddace 1981; Fujita et al. 1996; Fabian et al. 1997; Sakelliou & Ponman 2004; Fujita et al. 2008; Akamatsu et al. 2017).

Another probe of the diffuse ionised hot gas in the clusters and cluster pairs (more generally cluster systems) is the tSZ effect. Its amplitude measures the gas pressure, P_e, and is quantified by the Compton parameter y:

$$y = \frac{\sigma_T}{m_e c^2} \int P_e(l) \mathrm{d}l = \frac{\sigma_T}{m_e c^2} \int n_e(l) k_b T_e(l) \mathrm{d}l, \quad (1)$$

where σ_T is the Thomson cross-section, m_e the mass of the electron, c the speed of light, k_b the Boltzmann constant, and $n_e(l)$ and $T_e(l)$ the density and the temperature of the free electrons along the line of sight, respectively. The n_e dependence of the tSZ effect, compared with the n_e^2 dependence of the X-ray emission, makes the tSZ effect a good tracer of diffuse gas regions. The *Planck* survey (Planck Collaboration I 2011) provides tSZ maps over the whole of the extragalactic sky (Planck Collaboration XXII 2016). This has driven some recent studies on the inter-cluster filaments from tSZ data (e.g. Planck Collaboration VIII 2013).

In this study, we focus on cluster pairs and perform a multi-wavelength analysis with tSZ data from *Planck* and optical and near-infrared data from SDSS and WISE (Wright et al. 2010). We derive the properties of both the gas and the galaxies in the inter-cluster filament to probe its possible origin. In Sect. 2, we present the data used for the multi-wavelength study. We explain, in Sect. 3, our selection of the cluster pairs studied in this work. In Sects. 4 and 5, we focus on the pair A399-A401. In Sect. 4, we perform the analysis of the tSZ data and derive the extension of the filaments, their pressure and their density[1]. In Sect. 5, we explore the properties of the galaxies in the clusters A399 and A401, and in the inter-cluster filament. We discuss our results in Sect. 6 and present our conclusions in Sect. 7. Throughout this study, we adopt the *Planck* 2015 cosmological parameters of Planck Collaboration XIII (2016). In particular, all distances and scales are computed with $h = 0.6774$.

2. Data

2.1. Meta-catalogues of galaxy clusters

In order to identify systems of galaxy clusters with filaments, we use the publicly available SZ cluster database[2], which is composed of a union of tSZ cluster catalogues obtained with different instruments: *Planck*, ACT, SPT, Carma, and AMI (see references to the catalogues used on the database's website). The catalogue contains 2690 sources, and for 1681 sources which are identified as clusters, the redshifts and mass proxies M_{500} (defined in Planck Collaboration XXIX 2014) are available. The redshifts range is between $z_{min} = 0.011$ and $z_{max} = 1.7$ with a median value $z_{med} \sim 0.31$.

[1] I.e. pressure and density of the filaments.
[2] http://szcluster-db.ias.u-psud.fr/

2.2. Planck data

Planck (Planck Collaboration I 2011) was the third satellite to measure the CMB temperature anisotropies. It observed the full-sky more than five times in nine frequencies from 30 to 857 GHz with two instruments: HFI (High Frequency Instrument, Lamarre et al. 2010; Planck HFI Core Team et al. 2011) and LFI (Low Frequency Instrument, Bersanelli et al. 2010; Mennella et al. 2011). LFI covers the 30, 44, and 70 GHz bands with 33.29, 27.00, and 13.21 arcmin angular resolution and HFI the 100, 143, 217, 353, 545 and 857 GHz bands with 9.68, 7.30, 5.02, 4.94, 4.83 and 4.64 arcmin angular resolution, respectively.

The frequencies of *Planck* have been specifically chosen to measure the tSZ effect from galaxy clusters. Based on two component separation techniques, the *Planck* collaboration has constructed full-sky maps of the tSZ Compton parameter at a resolution of 10 arcmin using the six highest frequencies (Planck Collaboration XXII 2016). We checked that using either of the two maps does not alter our results. In the following, we thus use the *Planck* 2015 map from (Planck Collaboration XXII 2016) constructed with the Modified Internal Linear Combination Algorithm (MILCA; Hurier et al. 2013). This map[3] is in HEALPIX format (Górski et al. 2005), with $n_{side} = 2048$ and a pixel size $\theta_{pix} = 1.7$ arcmin.

2.3. WISE

The WISE satellite (Wright et al. 2010) surveyed the whole sky at wavelengths 3.4, 4.6, 12 and 22 μm, with angular resolutions of 6.1, 6.4, 6.5 and 12 arcsec, respectively. The All-WISE Source Catalog[4] contains positions, motion measurements, photometry and ancillary information for 747 634 026 sources detected on AllWISE Atlas Images. For our study, we use the profile-fitted photometry measurements of the $W1$ (3.4 μm), $W2$ (4.6 μm) and $W3$ (12 μm) bands, flagged as w1mpro, w2mpro and w3mpro in the All-WISE Source Catalog. The associated errors are flagged as w1sigmpro, w2sigmpro and w3sigmpro.

2.4. Photometric redshifts catalogues

In order to have access to redshift information, we use the union of two full-sky photometric redshift catalogues: 2MPZ and WISExSCOS.

The catalogue 2MPZ (Bilicki et al. 2014) is a cross-match of sources from the WISE, SuperCOSMOS, and 2MASS catalogue of extended sources. The 2MPZ catalogue contains around 10^6 nearby galaxies, with spectroscopic redshifts for one third of the galaxies and photometric redshifts for the other two thirds. The median redshift is $z_{med} \sim 0.08$, and the redshift dispersion is $\sigma_z \sim 0.012$. We refer the reader to Bilicki et al. (2014) for more information about the construction of the catalogue, including the discussion on the purity obtained after the cuts performed to clean the galaxy catalogue from stars, blending, or AGN contamination.

The catalogue WISExSCOS (Bilicki et al. 2016) is an extension of the 2MPZ catalogue. It is a cross-match of sources from WISE and SuperCOSMOS, and is deeper than 2MPZ. The median redshift of the galaxies in this catalogue is $z_{med} \sim 0.2$, and the redshift dispersion is $\sigma_z \sim 0.033$. Here again, we refer the

[3] The tSZ map is available at http://pla.esac.esa.int/pla/
[4] Available at http://wise2.ipac.caltech.edu/docs/release/allwise/expsup/sec1_3.html#src_cat

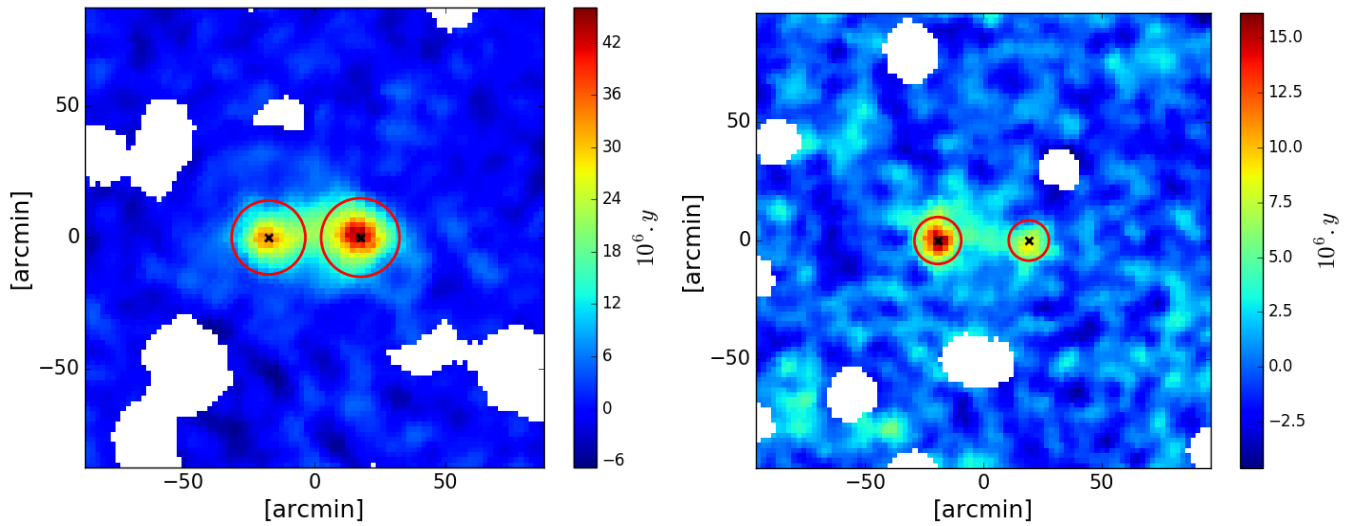

Fig. 1. Extracted masked patches of the *Planck* tSZ map of the two selected pairs. *Left*: the pair A399-A401. *Right*: the pair A21-PSZ2G 114.90-34.35. The red circles indicate radii r_{500} of the clusters and the white pixels are masked from the *Planck* Catalog of Compact Sources and from other clusters in the fields. The black crosses show the centres of the tSZ clusters.

reader to Bilicki et al. (2016) for more information about the catalogue.

2.5. SDSS

The SDSS has imaged one quarter of the sky in five optical bands: u, g, r, i and z. We use here the MPA–JHU catalogue, from the Max Planck Institute for Astrophysics and the Johns Hopkins University (Kauffmann et al. 2003; Brinchmann et al. 2004), where star formation rates (SFR) and stellar masses for 1 843 200 galaxies are provided. These data, based on the SDSS DR8 release, are publicly available[5] together with all details about the catalogue and the computations and fits of the galaxy physical properties. For our study, we extract from the catalogues the median values of SFR and stellar masses, flagged as SFR_TOT_P50 and LGM_TOT_P50, respectively.

3. Selection of galaxy cluster pairs

In our analysis, we select the cluster pairs based on the tSZ signal given that it is a priori a more appropriate tracer of the diffuse hot gas. We therefore base our selection of the cluster pairs both on the SZ catalogue of clusters and on the signal-to-noise ratio (S/N) of the tSZ signal between the pairs. In order to define the cluster region, we estimate the cluster extension r_{500}[6], defined as $r_{500} = \left(\frac{1}{500} 2GH_0{}^{-2}E(z)^{-2}M_{500}\right)^{\frac{1}{3}}$ (Aghanim et al. 2009), for the 1681 SZ clusters for which both redshift and mass estimate $M_{500}^{\rm SZ}$ are available.

Following Planck Collaboration VIII (2013), we apply three conditions to select the galaxy-cluster pairs. First, the two clusters need to be at the same redshift, second, the distance between the two clusters needs to be large enough to avoid blending effects, and finally, the significance of the tSZ signal in the inter-cluster region needs to be above 2σ. The two first empirical conditions were proposed by Planck Collaboration VIII (2013): $\Delta z < 0.01$, and considering the *Planck* tSZ map beam of 10 arcmin, 30 arcmin $< \theta_{\rm sep} <$ 120 arcmin. Here Δz is the redshift difference between the two clusters and $\theta_{\rm sep}$ is the angular distance separating the two clusters. This corresponds to projected distances between 3 and 40 Mpc. We find that a total of 71 cluster pairs satisfy the two conditions (Fig. 2). This is about three times more pairs than the selection based on clusters from the Meta-Catalog of X-ray detected Clusters (MCXC) catalogue (Piffaretti et al. 2011), performed in Planck Collaboration VIII (2013). About one third of the clusters in these pairs are Abell clusters (Abell et al. 1989), one third are *Planck* newly detected clusters, and the others are X-ray clusters from the MCXC catalogue or SZ clusters detected by SPT.

Since our aim is to study and characterise the filamentary gas between pairs of clusters, we consider the tSZ signal significance in terms of the S/N of the tSZ emission in the filament region, $S/N_{\rm fil}$. For each cluster pair, we extract patches of the *Planck* tSZ map of $s = 90$ pixels aside, centered on the mean of the two cluster positions, with a patch resolution $\theta_{\rm p}$ depending on the angular distance $\theta_{\rm sep}$ separating the two clusters: $\theta_{\rm p} = (5 \times \theta_{\rm sep})/s$. We rotate the image for convenience, and mask the tSZ signal at the positions of the *Planck* Catalog of Compact Sources (Planck Collaboration XXVIII 2014) and at those of the other tSZ sources in the fields, except in an area defined as the region encompassed within $3 \times r_{500}$ from the cluster centre. Figure 1 shows such a tSZ map with the red circles representing the r_{500} radii of the clusters, and the white pixels the masked regions. On these patches, we define the area of the potential inter-cluster filament as the cylinder between the minimum of the two r_{500} in the radial direction and between the two r_{500} in the longitudinal direction. We estimate the signal-to-noise ratio $S/N_{\rm fil} = (y_{\rm m,fil} - y_{\rm m,bkgd})/\sigma_{\rm bkgd}$, where $y_{\rm m,fil}$ is the mean tSZ signal in the area defining the filament, and $y_{\rm m,bkgd}$ and $\sigma_{\rm bkgd}$ are the tSZ signal and the standard deviation of the background area beyond the $3 \times r_{500}$ distance from the cluster centres.

We show in Fig. 2 the 71 cluster pairs that satisfy the two first conditions (redshift and angular separations). The areas and colours of the circles display the estimated $S/N_{\rm fil}$. Green open circles mark the pairs for which the S/N is greater than two. Among these, we choose to discard the cluster pairs belonging to larger and more complex super-clusters such as Shapley (Proust et al. 2006), or the pair containing the cluster A3395, a system known to host several groups (Lakhchaura et al. 2011; Planck Collaboration VIII 2013). We also finally remove the pair

[5] http://sdss.org

[6] r_{500} is defined as the radius of the sphere within which the cluster mean mass over-density is 500 times the critical density.

Table 1. Main properties of the selected pairs.

Cluster	RA (deg)	Dec (deg)	S/N_{SZ}	S/N_d	z	r_{500} (Mpc)	θ_{sep} (′)	θ_{sep} (Mpc)	S/N_{fil}	$S/N_{fil,d}$
A399	44.45	13.05	12.96	8.85	0.072	1.20	35.05	3.0	8.74	7.89
A401	44.73	13.57	19.66	9.74	0.074	1.30				
A21	5.15	28.67	9.36	6.19	0.094	1.07	38.5	4.2	2.53	2.08
PSZ2 G114.9	5.35	28.05	4.78	2.63	0.095	0.93				

Notes. Columns are: cluster names, tSZ positions in RA and Dec. S/Ns of the clusters in the SZ map (SZ cluster database) and in galaxy over-density (Sect. 5.2), redshifts, estimated radii r_{500}. The last four columns indicate the angular separation in arcmin and in Mpc, and the S/Ns of the filaments in the tSZ map (Sect. 3) and in galaxy over-density (Sect. 5.2).

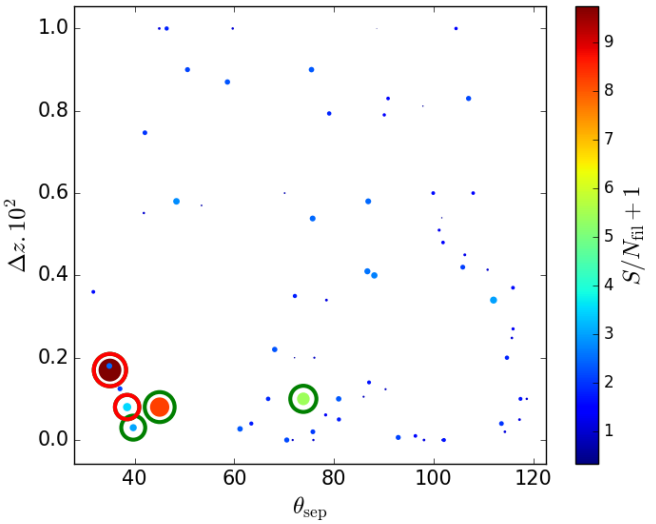

Fig. 2. Distribution of the 71 cluster pairs in the parameter space Δz-θ_{sep}. The areas and colours of the circles depend on S/N_{fil}. The pairs for which $S/N_{fil} > 2$ are shown with green open circles. The red open circles indicate the final selection after exclusion of pairs in complex systems.

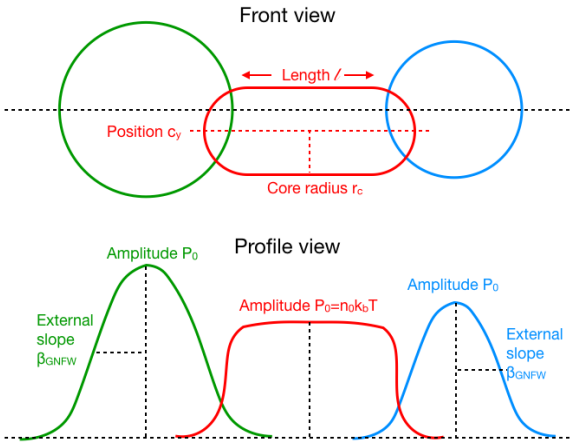

Fig. 3. Front and profile schematic views of the model: the two clusters in green and blue with two free parameters each, and the inter-cluster filament in red with three free parameters. The length of the filament l is fixed to the distance between the two $r_{500}/2$ of each cluster. A planar background with three free parameters is considered.

SPT J0655-5234–SPT J0659-5300, at redshift $z = 0.47$, with $S/N_{fil} = 2.03$. The redshift of this system is high, and thus the two catalogues used to study the galaxies in Sect. 5, with $z_{med} \sim 0.08$ and $z_{med} \sim 0.2$, lack statistics. A dedicated study of the removed pairs will be performed later. Eventually, we focus on two isolated pairs with a significant tSZ signal in their inter-cluster region (red open circles in Fig. 2): the pair A399-A401 at redshift $z \sim 0.073$ with $S/N_{fil} = 8.74$ and the newly associated pair A21-PSZ2 G114.09-34.34 at redshift $z \sim 0.094$ with $S/N_{fil} = 2.53$. Their main properties are presented in Table 1, and the patches of the *Planck* SZ map are shown in Fig. 1.

4. Gas properties from tSZ analysis

4.1. Model

In order to derive the gas properties of the inter-cluster filament, we model the entire system with four components: two clusters, one filament, and a planar background (Fig. 3). To model the galaxy clusters (blue and green components in Fig. 3), we choose to use the spherically symmetric Generalized Navarro Frenk & White (GNFW) pressure profile (Nagai et al. 2007; Arnaud et al. 2010; Planck Collaboration V 2013) given by:

$$P(r) = \frac{P_0}{\left(\frac{r}{r_s}\right)^{\gamma}\left[1+\left(\frac{r}{r_s}\right)^{\alpha}\right]^{(\beta_{GNFW}-\gamma)/\alpha}}, \quad (2)$$

where r is the radius, P_0 is the central pressure, $r_s = r_{500}/c_{500}$ is the characteristic radius, and $\gamma, \alpha, \beta_{GNFW}$ are the internal ($r < r_s$), intermediate ($r \sim r_s$), and external ($r > r_s$) slopes, respectively. All the parameters, but two, are fixed to the ones of the *universal profile* fitted by Planck Collaboration V (2013) on stacked tSZ clusters. The two parameters we let free are β_{GNFW} (related to the cluster extension) and P_0 (related to the Compton parameter y amplitude). These two parameters can be degenerate with each other, and with the parameters of the filament such as its length or its pressure (see Sect. 4.2).

The GNFW pressure profile was specifically developed to model the pressure distribution in galaxy clusters. As such it cannot be applied to filaments. In the absence of any physically motivated or established model of the inter-cluster filamentary gas, we choose a simple isothermal β-model (Cavaliere & Fusco-Femiano 1978), with a cylindrical geometry, to describe the pressure distribution in the radial direction of the filament:

$$n_e(r) = \frac{n_{e,0}}{\left(1+\left(\frac{r}{r_c}\right)^2\right)^{\frac{3}{2}\beta}}, \quad (3)$$

where r is the radius, $n_{e,0}$ is the central electron density in the filament, r_c the core radius and β the slope, fixed to 4/3 to model a non-magnetised filament (Ostriker 1964). Three parameters are let free: the central pressure in the filament $P_0 = n_0 \times k_b T$ (where T is the electron gas temperature), the core radius r_c (filament extension in the radial direction), and the position of the filament

Table 2. Best-fit parameters of the model derived from the MCMC.

A399		A401		Filament		
P_0(keV cm^{-3})	$\beta_{\rm GNFW}$	P_0(keV cm^{-3})	$\beta_{\rm GNFW}$	P_0(keV cm^{-3})	$r_{\rm c}$ (Mpc)	c_y (%)
$(1.54 \pm 0.04) \times 10^{-2}$	3.60 ± 0.04	$(2.27 \pm 0.04) \times 10^{-2}$	3.98 ± 0.03	$(2.84 \pm 0.27) \times 10^{-3}$	1.52 ± 0.09	51.24 ± 0.15

Notes. The best values are the median of the parameters distributions, and the error-bars are computed with the 16th and the 84th percentiles.

in the radial direction c_y (expressed as a percentage of the map size). The length of the filament in the horizontal direction l is fixed here to the distance between the two $r_{500}/2$ of each cluster to avoid any degeneracies between the parameters of the filament and those of the two clusters, and thus avoid any bias in the measurements of the pressures of the clusters.

Finally, a plane ($f(x, y) = ax + by + c$) is chosen to model the background; it corrects from possible residual gradient emission induced by large-scale contamination to the tSZ signal such as galactic dust emission.

4.2. Results for the pair A399-A401

We perform a Monte Carlo Markov chain (MCMC) analysis using the `python` algorithm `emcee` (Foreman-Mackey et al. 2013) on the pair A399-A401 to fit the ten free parameters to the most recent *Planck* tSZ map (Planck Collaboration XXII 2016). The resulting posterior parameter distributions are shown in Fig. 6.

All the parameters are well constrained. We first note the total absence of degeneracies between the three parameters of the background and the physical parameters of the model. This shows that for the cluster pair A399-A401 the physical properties that we measure, such as the pressures in the clusters or in the filament, are not biased by a potential large-scale contamination. An interesting point when looking at the correlations between the ten parameters is the degeneracies between the two parameters of the cluster model, $\beta_{\rm GNFW}$ and P_0. This reflects the fact that a high tSZ amplitude can be obtained by the combination of a high external slope and a small cluster extension. We do not see any obvious degeneracies with other parameters. Similarly to the cluster we also note a degeneracy between the two physical parameters of the filament central pressure and radial extension: $P_0 = n_0 \times k_{\rm b} T$ and $r_{\rm c}$.

From the MCMC analysis, we find the best-fit median central pressure in the filament is $P_0 = (2.84 \pm 0.27) \times 10^{-3}$ keV cm^{-3}, and the best-fit radius is $r_{\rm c} = 1.52 \pm 0.09$ Mpc, that is, $r_{\rm c} = 17.6 \pm 1.1$ arcmin. The filament's pressure obtained from our tSZ-only analysis is in perfect agreement with the value obtained with the density and the temperature measurements from the tSZ/X-rays analysis by Planck Collaboration VIII (2013): $P_0 = (2.6 \pm 0.5) \times 10^{-3}$ keV cm^{-3}. Assuming the most accurate temperature measured by Fujita et al. (2008) with Suzaku in X-rays, $k_{\rm b} T_{\rm X} = 6.5 \pm 0.5$ keV, we estimate the central density in the filament to be $n_0 = (4.3 \pm 0.7) \times 10^{-4}$ cm^{-3}, which is again in full agreement with the value $n_0 = (3.7 \pm 0.2) \times 10^{-4}$ cm^{-3} derived by Planck Collaboration VIII (2013) from their combined analysis of tSZ and X-ray signals. We compute the model (clusters + filament) using the best-fit parameters derived from the MCMC (see Table 2). The reduced chi-square value obtained from the comparison of the model to the tSZ map is $\chi^2 = 0.97$. We show the residual tSZ signal after subtracting the model (clusters + filament) in Fig. 4. It exhibits no significant tSZ emission between the clusters. Finally, we illustrate the good agreement between the model and the data by showing in Fig. 5 the model superimposed with the longitudinal cut in the tSZ map, across the two clusters.

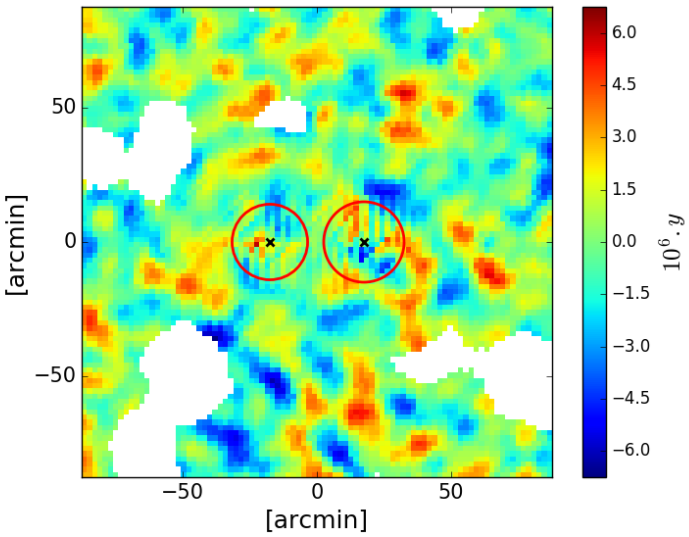

Fig. 4. Residual *Planck* tSZ map of the pair A399-A401 after subtracting the model (clusters + inter-cluster filaments) with the best-fit parameters from Table 2. The red circles represent the r_{500} radii of each cluster, and the black crosses their central positions.

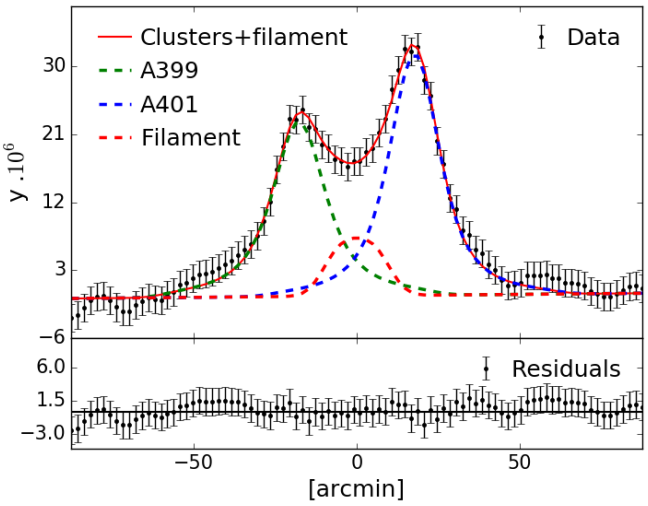

Fig. 5. Longitudinal cut across A399-A401 system. *Top panel*: the fuchsia line shows the *Planck* tSZ data. The red line is the model (clusters + inter-cluster filament) with the best-fit parameters from Table 2. The dotted green, blue, and red lines show the contributions of A399, A401, and of the inter-cluster filament, respectively. *Bottom panel*: residuals after subtracting the model (clusters + inter-cluster filament).

4.3. Results for the pair A21-PSZ2 G114.90-34.35

The newly associated pair A21-PSZ2 G114.90-34.35 shows hints of a tSZ signal at $S/N_{\rm fil} \sim 2.5$, associated with the

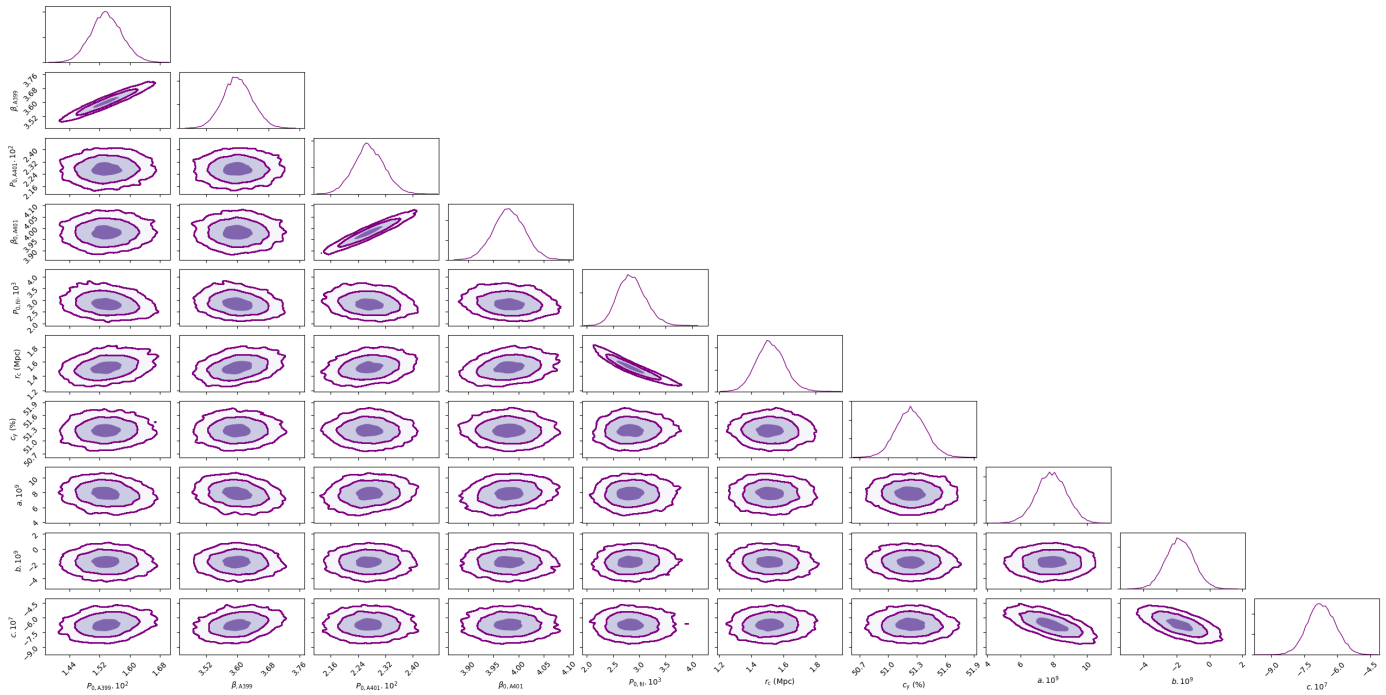

Fig. 6. Posterior parameter distributions from the MCMC analysis of the system A399-A401. The diagonal plots show the one-dimensional (1D) likelihood of the 11 parameters.

inter-cluster region. We perform the same analysis of the tSZ map as for A399-A401. Similarly, we find that the parameters P_0 and β_{GNFW} of the two clusters are degenerate. Considering the lower significance of the tSZ signal in this case, it is difficult to fit the parameters of the model with the MCMC analysis. Therefore, we further fixed the extension radius of the filament r_c. As we expect this parameter to be lower or equal to the clusters' extensions, we set it to the smallest r_{500} of the two clusters, here $r_c = 0.92$ Mpc or $r_c = 8.5$ arcmin. The deduced gas pressure of the filament is $P_0 = 1.6^{+0.7}_{-0.3} \times 10^{-3}$ keV cm^{-3}. In Fig. 7, we show the contributions of the three components of the system (clusters + inter-cluster filament) computed with the best-fit parameters from the MCMC analysis of the tSZ map and over-plotted on the longitudinal cut across the map. The reduced chi-square is $\chi^2 = 0.96$ indicating the good agreement between the model and the data.

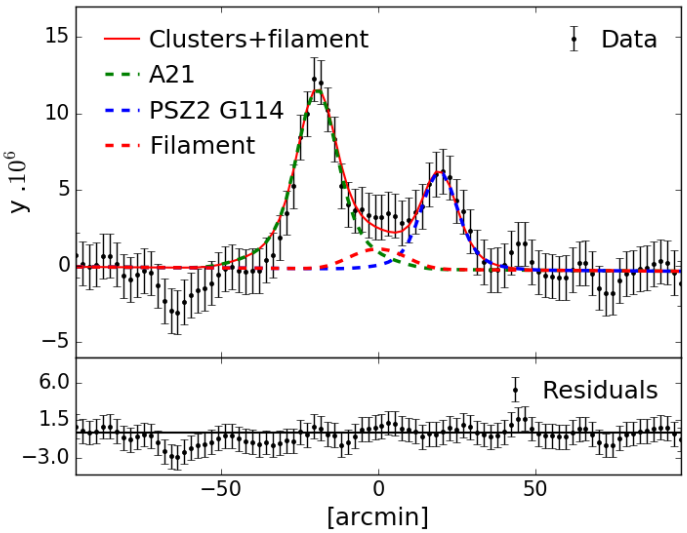

Fig. 7. Longitudinal cut across the A21-PSZ2 G114.90-34.35 system. The labels are the same as in Fig. 5.

5. Galaxy properties in the cluster pairs

X-ray and tSZ observations have allowed the detection of diffuse gas in between the clusters of the systems A399-A401 and A21-PSZ2 G114.90-34.35, and we have constrained the filament's properties with the tSZ signal from *Planck*. Here, we study the galaxies in the three components (clusters and filaments) of the two systems, and investigate the possible differences between their properties (types, SFRs, and stellar masses). We focus on the pair A399-A401 and summarise the main results of the pair A21-PSZ2 G114.90-34.35.

5.1. Selection for A399-A401

We use the photometric bands and photometric redshifts from SuperCosmos, WISE, and 2MASS. We follow Bilicki et al. (2016) who assume that the K band of 2MASS and the $W1$ band of WISE are equivalent for low redshift galaxies. In that way, the union catalogue provides us with redshifts for all galaxies with $W1 < 17$. We cross-match the resulting union catalogue and the All-WISE Source Catalog (following Bilicki et al. 2014, the matching distance is set to <3 arcsec). We then retrieve the source magnitudes in the bands $W1$, $W2$, and $W3$ and apply the k-correction factor $-2.5\log(1+z)$.

We first select all galaxies in the redshift range $\sim 0 < z <\sim 0.5$ within the field of the *Planck* tSZ map (see Fig. 1). This first selection represents 6487 galaxies. We then refine the selection in order to focus on galaxies likely to belong to the A399-A401 system. To do so, we select galaxies in the range $0.068 < z < 0.078$ which corresponds to redshifts between the lowest and highest redshifts of the cluster system plus and minus the velocity dispersion of the two clusters (Oegerle & Hill 2001). For simplicity and coherence with the tSZ analysis, we

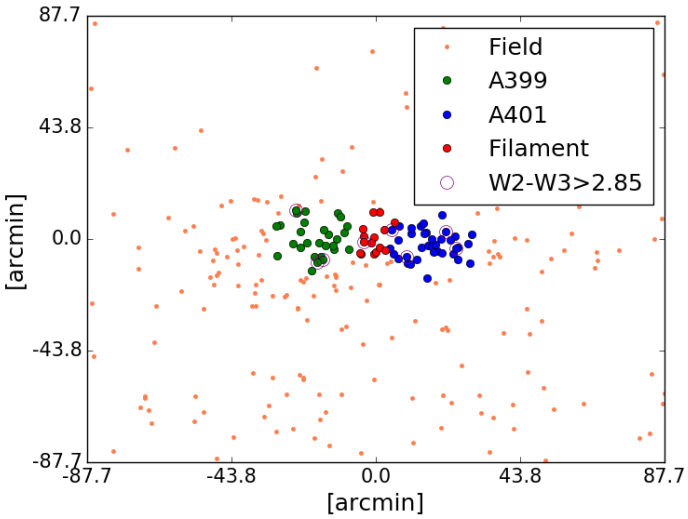

Fig. 8. The orange dots represent the galaxies in the field of A399-A401 in the redshift range $0.068 < z < 0.078$. The green dots are the galaxies selected to be in the galaxy cluster A399, the blue ones are the galaxies selected to be in A401, and the red dots are those of the inter-cluster filament. The purple circles indicate galaxies with $W2 - W3 > 2.85$.

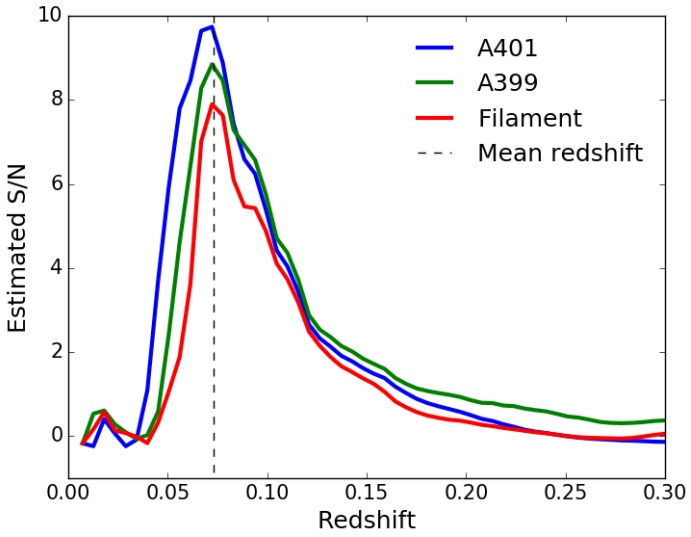

Fig. 9. Distributions of the S/Ns of over-densities for the three components of the system A399-A401. The blue line corresponds to cluster A401, the green line to A399, and the red one to the inter-cluster filament region.

assume that member galaxies are defined as those within an area of radius r_{500}, centred on the tSZ cluster positions. The galaxies which belong to the inter-cluster filament are defined to be spatially contained between the positions c_y plus or minus the core radius r_c, both parameters fitted with the MCMC in Sect. 4. Galaxies outside these regions are considered as field galaxies. We show in Fig. 8 the selected galaxies in the different components of the system A399-A401. The orange dots are for the field galaxies whereas the green, blue, and red dots represent galaxies belonging to A399, A401, and to the inter-cluster filament, respectively.

5.2. Galaxy over-densities

We have implemented a three-dimensional (3D) Delaunay Tesselation Field Estimator (3D DTFE in `python`[7]; Bernardeau & van de Weygaert 1996; Schaap & van de Weygaert 2000; Schaap 2007 to estimate a 3D galaxy density in the field of A399-A401. We compute the over-density based on all galaxies, such that $\sim 0 < z < \sim 0.5$, within the field of the *Planck* tSZ map. For each redshift bin of width $\delta z = 0.005$, we compute the mean over-density in the three regions defining the components of the system (i.e. clusters and filament). We compare the mean density in the galaxy cluster regions and in the filament to the mean density of the background and its standard deviation. In Fig. 9, we show the distribution of the over-density S/N as a function of redshift for the three components of the system. It is clear that the S/Ns in the regions of the two galaxy clusters and the one of the inter-cluster filament peak at the mean redshift of the system. We conclude that we detect a structure with a confidence, $S/N_{\rm fil} \sim 8$, comparable to the tSZ signal.

5.3. Optical properties

A standard method to identify collapsed structures (e.g. galaxy clusters) from galaxy optical properties is to search for a red sequence (Visvanathan & Sandage 1977; Gladders & Yee 2000; Rykoff et al. 2014). Indeed, galaxies in clusters are expected to

[7] https://github.com/vicbonj/pydtfe

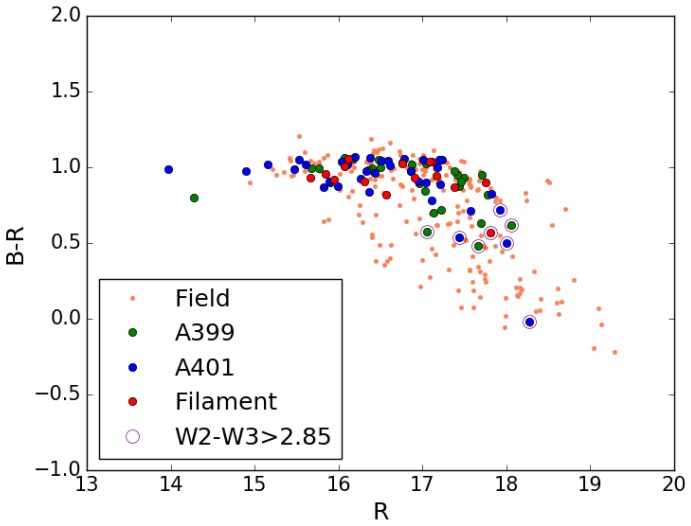

Fig. 10. Colour–magnitude diagram using B and R photometric bands from SuperCOSMOS. The labels are the same as those in Fig. 8.

be red and dead at low redshift, with the 4000 Å-break being the main feature in their spectra. The colours of the galaxies in a cluster computed with two magnitudes surrounding this break will be roughly the same, and a linear feature will form in the colour–magnitude diagram, referred to as the red sequence.

As the 4000 Å-break is between the magnitudes B and R for low-redshift galaxies, we use the photometric bands of SuperCOSMOS to produce the colour–magnitude diagram $B - R$ versus R, for the galaxies in the system A399-A401. The resulting plot is shown Fig. 10. We note that the galaxies in the three components of the system tend to align on a red sequence. An interesting point is that the galaxies in the filament region are also following the same red sequence as the one in the clusters. Below, we investigate that point and confirm that trend by estimating galaxy types with infrared properties.

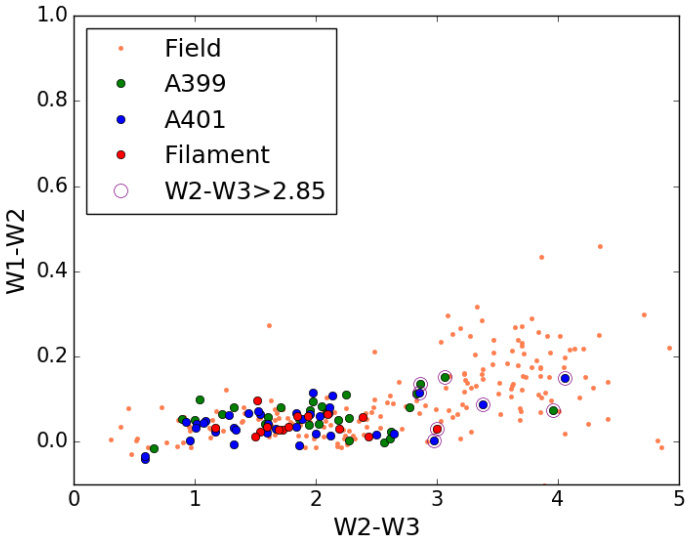

Fig. 11. Colour–colour diagram from the photometric bands $W1$, $W2$, and $W3$. The labels are the same as those in Fig. 8.

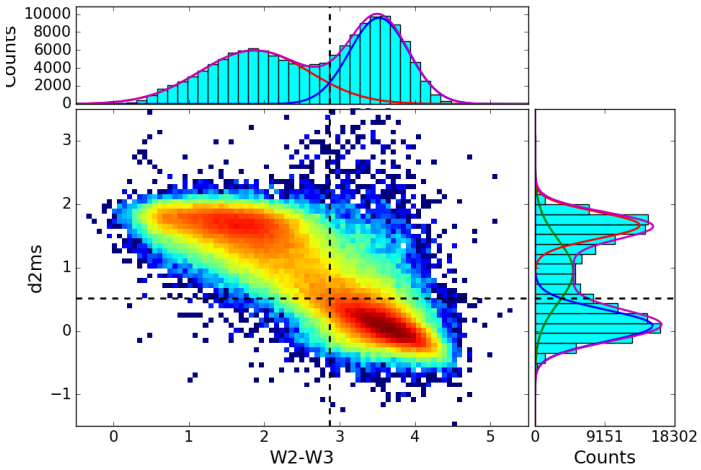

Fig. 12. 2D histogram of the projected distance to the main sequence in the SFR/mass plane vs. the $W2-W3$ colour, for the 148 685 galaxies of the SDSS MPA-JHU DR8 field cross-matched with the union catalogue of photometric redshifts. *Top*: histogram of the colour $W2-W3$. We have fitted two Gaussians for the early-type galaxies in red, and for the late-type galaxies in blue. *Right*: histogram of the projected distance to the main sequence. We have fitted three Gaussians: red and dead (in red), star-forming (in blue), and green valley (in green) galaxies. We set a threshold at $W2-W3 = 2.85$ (solid black line) to separate star-forming galaxies.

5.4. Infrared properties

As shown in Lee et al. (2015), there are two main populations of galaxies with different properties in infrared: early-type and late-type galaxies. The early-type galaxies are massive and passive, composed mostly of elliptical E and spiral S0, which lay on an optical red sequence. They are "red and dead" or in the green valley (transiting from star-forming to passive). Late-type galaxies are mainly star-forming, blue, and spiral galaxies. Wright et al. (2010) have used colour-colour diagrams based on the $W1-W2$ and $W2-W3$ near-infrared colours from WISE to differentiate between galaxy morphologies: elliptical or spiral galaxies. Elliptical galaxies were found to be mainly located between $0.5 < W2-W3 < 1.5$ and $-0.1 < W1-W2 < 0.3$, and spirals between $1 < W2-W3 < 4.5$ and $-0.1 < W1-W2 < 0.7$ (see Fig. 12 in Wright et al. 2010). In a similar way, we use the bands $W1$, $W2$, and $W3$ and we show that all galaxies in the A399-A401 system (clusters + filament) are located in the two regions defining elliptical and spiral galaxies (see Fig. 11).

We further use the $W2-W3$ colour to segregate late-type and early-type galaxies. To do so, we cross-match the SDSS MPA-JHU DR8 catalogue with the union catalogue of photometric redshifts. For each of the 148 685 galaxies, we use the SFR and stellar mass provided in the catalogues to evaluate the projected distance, noted d2ms, in the SFR/mass plane to the SFR/mass relation of the main sequence for star-forming galaxies given by Brinchmann et al. (2004). We show in Fig. 12 the histogram of the distances as compared with the histogram of the $W2-W3$ colours for the same galaxies. The black dotted line in Fig. 12 represents the $W2-W3 = 2.85$ colour-cut above which the galaxies are star-forming ones, with projected distances to the main sequence d2ms ~0. Throughout the plot, we display the star-forming galaxies with purple circles. The threshold at W2-W3=2.85 between early and late-type galaxies agrees well with the one found by Alatalo et al. (2014) between the green valley (early types) and the star-forming galaxies (late types). The galaxies which align on the red sequence in Fig. 10 are the same as those belonging to the early-type population (as defined by $W2-W3 < 2.85$) in Fig. 11.

These consistent results indicate that there is no obvious segregation between the galaxies in the clusters and in the inter-cluster filament. Most of the galaxies in the three components of the A399-A401 system are passive, mainly composed of elliptical E and spiral S0.

5.5. SFRs and stellar masses

The infrared luminosity traces the SFRs and the stellar masses of galaxies (Calzetti et al. 2007; Cluver et al. 2014), as the dust heated by young stars (indicators of the SFR) and old stars (indicators of the stellar mass) re-emits in the infrared wavelengths. Cluver et al. (2014) have fitted correlations between the SFR and the luminosity in the $W3$ band for star-forming galaxies, and between the stellar mass, the luminosity in the $W1$ band, and the colour $W1-W2$.

In the following, we estimate the SFRs and stellar masses for passive galaxies in order to confirm the results obtained from the optical and infrared colour properties. To do so, we develop a method based on a machine learning algorithm[8], trained with the SDSS MPA-JHU DR8 catalogue cross-matched with the union catalogue of photometric redshifts (Bonjean et al., in prep.). To estimate the SFRs with the neural network, we give as input the luminosity in the $W3$ band, the colours $W1-W2$ and $W2-W3$, the redshifts, and the SFR from the SDSS MPA-JHU DR8 catalogue. For the stellar masses, we give as input the luminosity in the $W1$ band, the colours $W1-W2$ and $W2-W3$, and the stellar masses from the SDSS MPA-JHU DR8 catalogue.

We estimate with the neural network, the SFRs, and the stellar masses of the galaxies in the system A399-A401, and compare them, in Fig. 13, to the ones of the SDSS field and to the main sequence of star-forming galaxies fitted by Brinchmann et al. (2004). The contours represent the galaxies of the SDSS field used to train the machine learning algorithm on the same slice of redshift as the selected field, $0.068 < z < 0.078$. We confirm here that almost all the galaxies in the three components of the system are passive. We also find very good

[8] `MLPRegressor` in `scikit-learn` library in `python`

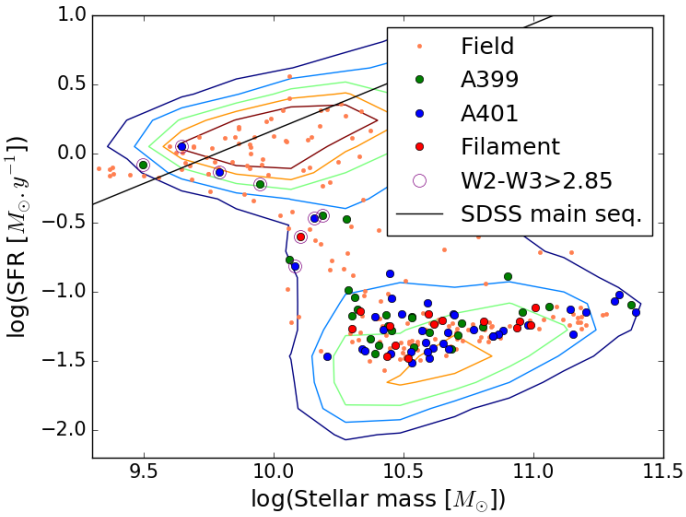

Fig. 13. SFRs versus stellar masses for the galaxies in the field of A399-A401. The labels are the same as those in Fig. 8. The black line corresponds to the main sequence fitted by Brinchmann et al. (2004) on the SDSS MPA-JHU galaxies. The contours represent the galaxies from the cross-match between the union catalogue and the SDSS MPA-JHU DR8 catalogue, in the redshift range $0.068 < z < 0.078$.

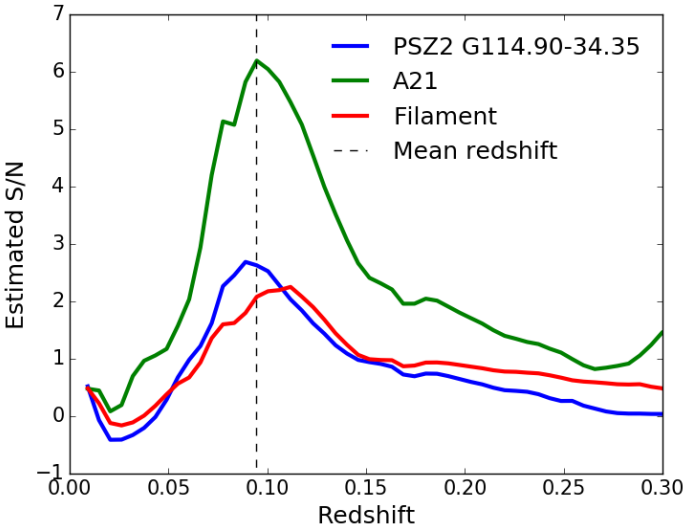

Fig. 14. Distribution of the S/Ns of over-densities for the three components of the system A21-PSZG114.90-34.35. The blue line corresponds to PSZG114.90-34.35, the green line to A21 and the red line to the region between the two clusters.

agreement between estimated early-type galaxies with the proposed threshold at $W2 - W3 > 2.85$, and the location of active galaxies in the main sequence diagram, as in the colour-colour and in the colour–magnitude diagrams.

5.6. Results for the pair A21-PSZ2 G114.90-34.35

We compute the 3D density field in the region of the pair A21-PSZ2 G114.90-34.35. The significance of an over-density of galaxies between the two clusters is lower than in the A399-A401 case (see Fig. 14). We find, in the inter-cluster region, an over-density with a S/N of about 2.5. However due to the lack of statistics for this cluster system, we cannot study the galaxy properties and conclude on their nature.

6. Discussion

First observations of the pair A399-A401 in the X-rays with the *Einstein* telescope (Ulmer & Cruddace 1981) did not show any evidence of signal between the two clusters (Karachentsev & Kopylov 1980; Ulmer & Cruddace 1981) because of the high background noise. It is only with ASCA and ROSAT that Fujita et al. (1996) and Fabian et al. (1997) detected an excess of X-ray emission that they associated with a diffuse gas in between the two clusters. Given that the two clusters, A399 and A401, lack cooling-flows and contained diffuse radio halos (Murgia et al. 2010), the gas between the two clusters was interpreted as the result of a post-merger (Fabian et al. 1997). Alternatively, Fujita et al. (1996) suggested a pre-merger scenario to explain the origin of the X-ray emission, since the temperatures of the gas and the two clusters were of the same order. Another explanation for the presence of a filament between the two clusters is that the whole system was formed at the same time and that the gas in the inter-cluster region is a relic of a cosmic filament, as proposed by Akamatsu et al. (2017). The higher quality *XMM-Newton* data from the four pointing observations of A399-A401 permitted to measure the gas properties of the two clusters and of the filament between them (Sakelliou & Ponman 2004). This revealed both the absence of big anomalies in the temperature profiles and the relaxed nature of the clusters, with no significant offset between the positions of their BCGs and the central positions of the X-ray emissions. Sakelliou & Ponman (2004) further interpreted the radio halos in the two clusters as relics of past minor mergers in each cluster. All this evidence, strongly favours a pre-merger scenario that has been reinforced by the Suzaku observations conducted by Fujita et al. (2008) who found a high metallicity in the inter-cluster region, 0.2 $Z_\odot$, of the same order of the metallicity as in the clusters, indicative of superwinds that transported metals from the clusters to the inter-cluster region.

In order to investigate the different scenarios and discriminate between them, it is necessary to fully characterise the properties of the inter-cluster filament. In the present study, we thus complete the analysis of the system A399-A401 by exploring the tSZ signal and the galaxy properties. We confirm the presence of gas between the two clusters A399 and A401 with a significance of approximately 8.5σ from the *Planck* tSZ data alone. We have measured the pressure of the inter-cluster gas, $P_0 = (2.8 \pm 0.27) \times 10^{-3}$ keV cm^{-3}, in agreement with the pressure computed with the density and the temperature fitted from the combined tSZ/X-rays analysis by Planck Collaboration VIII (2013), $P_0 = (2.6 \pm 0.5) \times 10^{-3}$ keV cm^{-3}. Using the most accurate gas temperature of Fujita et al. (2008), $k_\mathrm{b} T_\mathrm{X} = 6.5 \pm 0.5$ keV, we have further estimated a central density of $n_0 = (4.3 \pm 0.7) \times 10^{-4}$ cm^{-3}, in agreement with Planck Collaboration VIII (2013).

We note that Akamatsu et al. (2017) have also studied the geometry of the filament between A399 and A401. They consider a uniform density along the line of sight and estimate a Compton parameter in the filament, $y = 14.5 \pm 1.8 \left(\frac{l}{\mathrm{Mpc}}\right)^{0.5} \times 10^{-6}$, where l is an effective depth of the filament along the line of sight. Comparing the obtained Compton parameter with a weight-averaged y parameter in the tSZ map (roughly estimated at $y = 14\text{–}17 \times 10^{-6}$ in Planck Collaboration VIII 2013) they deduce an effective density $n_0 = 3.1 \times 10^{-4}$ cm^{-3} and the effective depth $l = 1.1$ Mpc. Akamatsu et al. compare this depth to the size of the filament in the radial direction, ~2.6 Mpc (compatible with our result, a size of 3.0 ± 0.2 Mpc), and conclude that the filament is flattened. Following their method, we focus on the very central region of the filament (within 2′ of the longitudinal axis)

and estimate a Compton parameter $y = 17.2 \pm 1.3 \left(\frac{l}{\mathrm{Mpc}}\right)^{0.5} \times 10^{-6}$, with $k_\mathrm{b} T_\mathrm{X} = 6.5 \pm 0.5$ keV and $n_0 = 3.3 \left(\frac{l}{\mathrm{Mpc}}\right)^{-0.5} \times 10^{-4}$ cm^{-3} (see their Fig. 7). We compare this to the value of the tSZ map, $y = 22.2 \pm 1.8 \times 10^{-6}$, and estimate an effective depth $l = 1.7 \pm 0.5$ Mpc. This value suggests that the shape of the filament is consistent with a cylinder, compatible with our hypothesis. However, we note that these computations of the filament depth l strongly depend on the model of the electron density and on the assumed value of y.

The re-analysis of the Suzaku data by Akamatsu et al. (2017) has shown hints of a shock in the direction parallel to the one linking the two clusters. Such a shock would be incompatible with a merger scenario of two clusters only, since numerical simulations predict shocks in the radial direction (Akahori & Yoshikawa 2008). This suggests the pre-existing cosmic filament, a hypothesis supported by Planck Collaboration VIII (2013). Our study is complementary and brings additional information on the scenario. The tSZ emission traces and detects diffuse gas, with a density one order of magnitude below the mean densities in the clusters. In addition, we detect a galaxy over-density between the clusters A399 and A401 with a significance of approximately 8σ. The colour–colour and colour–magnitude analyses of the galaxies selected in the system show that they are passive, early type, and red and dead. We do not observe any segregation between the galaxies belonging to the three components of the system. The properties of the galaxies in the A399-A401 system are those of the typical populations of galaxies in clusters or in dense collapsed structures. This contrasts with the results showing a large fraction of star-forming galaxies in intermediate-density environments such as filaments (Gallazzi et al. 2009; Edwards et al. 2010). It suggests that the mechanisms by which galaxies can undergo an enhancement of star formation (e.g. mergers, harassment, ram pressure, etc.) are less/not efficient in the A399-A401 system.

7. Conclusion

We have performed a tSZ-based selection of galaxy-cluster pairs showing hints of tSZ signal potentially associated with inter-cluster filaments. Among the 71 pairs satisfying our selection criteria on redshift and angular distance separations, we have selected the systems at the highest significance: A399-A401 at redshift $z = 0.073$ with $S/N_\mathrm{fil} = 8.74$ and A21-PSZ2 G114.90-34.35 at redshift $z = 0.094$ with $S/N_\mathrm{fil} = 2.53$. For these two systems, we performed a multi-wavelength analysis that allowed us to constrain the gas properties, obtain the galaxy types, and measure their SFRs and stellar masses in the three components of the system: the two clusters and the inter-cluster filament.

For the most significant pair, A399-A401, we measure a gas pressure in the inter-cluster filament, $P_0 = (2.84 \pm 0.27) \times 10^{-3}$ keV cm^{-3}, in agreement with previous studies but better constrained. We cannot identify any significant difference in the star-formation activity between the galaxies of the clusters and the galaxies of the inter-cluster filament: they all seem passive and red and dead. Our analysis of the galaxy properties weakens the post-merger hypothesis which was already disfavoured by the lack of a big offset between the positions of the BCGs and the centres of the X-ray emissions. Our findings, alternatively, favour the scenario in which the gas between the two clusters is associated with a cosmic filament. The gas is collapsing, smoothly compressed, and heated by the future collision of the two clusters A399 and A401. The current data are however not deep enough to accurately measure the effect of environmental quenching in the filament that connects the two clusters.

On the newly associated pair of clusters A21-PSZ2 G114.90-34.35, we detect an inter-cluster filament at 2.5σ from the analysis of the *Planck* tSZ map and we find the same significance in the 3D galaxy density field. However, we lack statistics to conduct a study on galaxy properties in the three components of this pair of clusters.

Dedicated observations in the X-rays, with a higher-resolution tSZ instrument, and optical or near-infrared wide-field spectroscopic data will be necessary in order to confirm the presence of inter-cluster filaments from our selection of galaxy-cluster pairs and/or perform a comprehensive combined analysis of their properties to study their origin and link to the cosmic web.

Acknowledgements. The authors acknowledge useful comments from an anonymous referee and fruitful discussions with M. Langer, G. Hurier, E. Pointecouteau, and C. de Boni. This work has received support from PI Invitation Program of Institute for Advanced Research, Nagoya University. This publication is based on observations obtained with *Planck* (http://www.esa.int/Planck), an ESA science mission with instruments and contributions directly funded by ESA Member States, NASA, and Canada. It made use of the SZ-Cluster Database operated by the Integrated Data and Operation Center (IDOC) at the Institut d'Astrophysique Spatiale (IAS) under contract with CNES and CNRS. It also used data obtained from the SuperCOSMOS Science Archive, prepared and hosted by the Wide Field Astronomy Unit, Institute for Astronomy, University of Edinburgh, which is funded by the UK Science and Technology Facilities Council. This publication makes use of data products from the Wide-field Infrared Survey Explorer, which is a joint project of the University of California, Los Angeles, and the Jet Propulsion Laboratory/California Institute of Technology, funded by the National Aeronautics and Space Administration. This research made use of Astropy, the community-developed core Phyton package (Astropy Collaboration et al. 2013) and matplotlib library (Hunter et al. 2007). This project has received funding from the European Research Council (ERC) under the European Union's Horizon 2020 research and innovation programme grant agreement ERC-2015-AdG 695561.

References

Abell, G. O., Corwin, H. G., Jr., & Olowin, R. P. 1989, ApJS, 70, 1
Aghanim, N., da Silva, A. C., & Nunes, N. J. 2009, A&A, 496, 637
Akahori, T., & Yoshikawa, K. 2008, PASJ, 60, L19
Akamatsu, H., Fujita, Y., Akahori, T., et al. 2017, A&A, 606, A1
Alatalo, K., Cales, S. L., Appleton, P. N., et al. 2014, ApJ, 794, L13
Alpaslan, M., Robotham, A. S. G., Driver, S., et al. 2014, MNRAS, 438, 177
Arnaud, M., Pratt, G. W., Piffaretti, R., et al. 2010, A&A, 517, A92
Astropy Collaboration, Robitaille, T. P., Tollerud, E. J., et al. 2013, A&A, 558, A33
Bernardeau, F., & van de Weygaert, R. 1996, MNRAS, 279, 693
Bersanelli, M., Mandolesi, N., Butler, R. C., et al. 2010, A&A, 520, A4
Bilicki, M., Jarrett, T. H., Peacock, J. A., Cluver, M. E., & Steward, L. 2014, ApJS, 210, 9
Bilicki, M., Peacock, J. A., Jarrett, T. H., et al. 2016, ApJS, 225, 5
Brinchmann, J., Charlot, S., White, S. D. M., et al. 2004, MNRAS, 351, 1151
Calzetti, D., Kennicutt, R. C., Engelbracht, C. W., et al. 2007, ApJ, 666, 870
Cavaliere, A., & Fusco-Femiano, R. 1978, A&A, 70, 677
Cluver, M. E., Jarrett, T. H., Hopkins, A. M., et al. 2014, ApJ, 782, 90
Dolag, K., Meneghetti, M., Moscardini, L., Rasia, E., & Bonaldi, A. 2006, MNRAS, 370, 656
Durret, F., Márquez, I., Acebrón, A., et al. 2016, A&A, 588, A69
Eckert, D., Jauzac, M., Shan, H., et al. 2015, Nature, 528, 105
Edwards, L. O. V., Fadda, D., Biviano, A., & Marleau, F. R. 2010, AJ, 139, 434
Elbaz, D., Daddi, E., Le Borgne, D., et al. 2007, A&A, 468, 33
Epps, S. D., & Hudson, M. J. 2017, MNRAS, 468, 2605
Fabian, A. C., Peres, C. B., & White, D. A. 1997, MNRAS, 285, L35
Fadda, D., Biviano, A., Marleau, F. R., Storrie-Lombardi, L. J., & Durret, F. 2008, ApJ, 672, L9
Foreman-Mackey, D., Hogg, D. W., Lang, D., & Goodman, J. 2013, PASP, 125, 306
Fujita, Y., Koyama, K., Tsuru, T., & Matsumoto, H. 1996, PASJ, 48, 191
Fujita, Y., Tawa, N., Hayashida, K., et al. 2008, PASJ, 60, S343
Gallazzi, A., Bell, E. F., Wolf, C., et al. 2009, ApJ, 690, 1883

Gladders, M. D., & Yee, H. K. C. 2000, AJ, 120, 2148
Górski, K. M., Hivon, E., Banday, A. J., et al. 2005, ApJ, 622, 759
Guennou, L., Adami, C., Ulmer, M. P., et al. 2010, A&A, 523, A21
Hunter, J. D. 2007, Comput. Sci. Eng., 9, 3
Hurier, G., Macías-Pérez, J. F., & Hildebrandt, S. 2013, A&A, 558, A118
Karachentsev, I. D., & Kopylov, A. I. 1980, MNRAS, 192, 109
Kauffmann, G., Heckman, T. M., White, S. D. M., et al. 2003, MNRAS, 341, 33
Lakhchaura, K., Singh, K. P., Saikia, D. J., & Hunstead, R. W. 2011, ApJ, 743, 78
Lamarre, J.-M., Puget, J.-L., Ade, P. A. R., et al. 2010, A&A, 520, A9
de Lapparent, V., Geller, M. J., & Huchra, J. P. 1986, ApJ, 302, L1
Lee, G.-H., Hwang, H. S., Lee, M. G., et al. 2015, ApJ, 800, 80
Martínez, H. J., Muriel, H., & Coenda, V. 2016, MNRAS, 455, 127
Mennella, A., Bersanelli, M., Butler, R. C., et al. 2011, A&A, 536, A3
Murgia, M., Govoni, F., Feretti, L., & Giovannini, G. 2010, A&A, 509, A86
Nagai, D., Vikhlinin, A., & Kravtsov, A. V. 2007, ApJ, 655, 98
Navarro, J. F., Frenk, C. S., & White, S. D. M. 1995, MNRAS, 275, 56
Oegerle, W. R., & Hill, J. M. 2001, AJ, 122, 2858
Ostriker, J. 1964, ApJ, 140, 1056
Piffaretti, R., Arnaud, M., Pratt, G. W., Pointecouteau, E., & Melin, J.-B. 2011, A&A, 534, A109
Planck Collaboration I. 2011, A&A, 536, A1
Planck Collaboration V. 2013, A&A, 550, A131
Planck Collaboration VIII. 2013, A&A, 550, A134
Planck Collaboration XVI. 2014, A&A, 571, A16
Planck Collaboration XXVIII. 2014, A&A, 571, A28
Planck Collaboration XXIX. 2014, A&A, 571, A29
Planck Collaboration XIII. 2016, A&A, 594, A13
Planck Collaboration XXII. 2016, A&A, 594, A22
Planck HFI Core Team, Ade, P. A. R., Aghanim, N., et al. 2011, A&A, 536, A4
Proust, D., Quintana, H., Carrasco, E. R., et al. 2006, A&A, 447, 133
Rykoff, E. S., Rozo, E., Busha, M. T., et al. 2014, ApJ, 785, 104
Sakelliou, I., & Ponman, T. J. 2004, MNRAS, 351, 1439
Schaap, W. E. 2007, Ph.D. Thesis, Kapteyn Astronomical Institute
Schaap, W. E., & van de Weygaert, R. 2000, A&A, 363, L29
Springel, V., White, S. D. M., Jenkins, A., et al. 2005, Nature, 435, 629
Sunyaev, R. A., & Zeldovich, Y. B. 1969, Nature, 223, 721
Tempel, E., Stoica, R. S., Martínez, V. J., et al. 2014, MNRAS, 438, 3465
Teyssier, R., Pires, S., Prunet, S., et al. 2009, A&A, 497, 335
Ulmer, M. P., & Cruddace, R. G. 1981, ApJ, 246, L99
Visvanathan, N., & Sandage, A. 1977, ApJ, 216, 214
Vogelsberger, M., Genel, S., Springel, V., et al. 2014, MNRAS, 444, 1518
Wright, E. L., Eisenhardt, P. R. M., Mainzer, A. K., et al. 2010, AJ, 140, 1868
York, D. G., Adelman, J., Anderson, J. E., Jr., et al. 2000, AJ, 120, 1579
Zhang, Y., Dietrich, J. P., McKay, T. A., Sheldon, E. S., & Nguyen, A. T. Q. 2013, ApJ, 773, 115